

## EMRIs in Kerr Spacetime: The Role of Inclination Diffusion

Yael Alush,<sup>1, 2</sup> Nicholas C. Stone,<sup>1, 2</sup> and Scott A. Hughes<sup>3</sup>

<sup>1</sup>Racah Institute of Physics, The Hebrew University, Jerusalem, 91904, Israel

<sup>2</sup>Department of Astronomy, University of Wisconsin, Madison, WI, 53706

<sup>3</sup>Department of Physics and MIT Kavli Institute, MIT, Cambridge, MA 02139 USA

### ABSTRACT

Extreme mass ratio inspirals (EMRIs) are expected to be a major source of gravitational waves (GWs) for the future Laser Interferometer Space Antenna (LISA). An EMRI occurs when a compact object slowly inspirals into a massive black hole (MBH), driven by the emission of gravitational radiation. The classical formation channel involves repeated two-body interactions within dense nuclear star clusters. However, both EMRI event rates and their orbital parameters remain highly uncertain. A major source of this uncertainty is the poorly constrained ratio between gradual inspiral EMRIs and direct plunges, which do not produce detectable GWs. While most studies of astrophysical EMRI production focus on the Schwarzschild limit, previous work examining the Kerr metric found that the spin of the central MBH can significantly affect the EMRI-to-plunge ratio. This enhancement depends sensitively on orbital inclination, yet earlier studies held inclination fixed. In this work, we develop the mathematical framework describing inclination evolution driven by two-body encounters. By implementation Monte Carlo simulations, we show that initially prograde orbits may evolve into retrograde states, thereby converting potential EMRIs into plunges or vice versa. We estimate the EMRI-to-plunge ratio and find that MBH spin enhances the EMRI rate. Additionally, even in the non-spinning case, modeling the orbits as relativistic geodesics rather than Newtonian Keplerian trajectories increases the number of EMRIs. These results demonstrate that the commonly adopted assumptions of fixed inclination and Keplerian dynamics lead to substantial inaccuracies in EMRI rate estimates.

### 1. INTRODUCTION

The first discoveries of Advanced LIGO inaugurated the era of gravitational wave (GW) astronomy (Abbott et al. 2016), opening a window on previously unobserved black hole (BH) populations (Abbott et al. 2023) and enabling novel strong-field tests (Abbott et al. 2016) of general relativity (GR). In the 2030s, the launch of space-based interferometers such as *LISA* and *TianQin/Taiji* will extend this window to lower frequencies (Danzmann & LISA Study Team 1996; Luo et al. 2016; Amaro-Seoane 2018) sensitive to massive black holes (MBHs). MBH-MBH mergers will provide the highest signal-to-noise ratios (SNRs in the thousands are likely; Valiante et al. 2021) out of all GWs seen in the *LISA* band, but it may ultimately be the slower inspiral of a stellar mass compact object (CO) into an MBH that provides the strongest tests of GR. These extreme mass

ratio inspirals (EMRIs; Ryan 1995) will stay in the *LISA* band for up to  $\sim 10^5$  cycles (Babak et al. 2017), accumulating an unprecedented degree of phase and timing information and therefore offering exquisite sensitivity to small deviations from GR (Yunes et al. 2012; Speri et al. 2024) or the Kerr metric (Ryan 1997; Collins & Hughes 2004); see Barausse et al. (2020) for a broad review. The astrophysics of EMRIs, however, remain highly uncertain.

Because classical EMRIs are electromagnetically dark, present-day estimates for their event rates and parameters are ultimately theoretical and subject to large uncertainties. Despite some Milky Way constraints (Hailey et al. 2018; Generozov et al. 2018), the population of nuclear stellar mass BHs is largely unknown outside our Galaxy. More fundamentally, it is currently unclear what is the dominant mechanism for feeding stellar mass BHs to MBHs. Most past work on this subject has focused on scatterings into the MBH loss cone (Cohn &

Corresponding author: Yael Alush  
yael.alush@mail.huji.ac.il

Kulsrud 1978): a conical region of velocity space<sup>1</sup> inside of which a test BH’s pericenter falls inside a critical value that would trigger its capture by the MBH (Hils & Bender 1995; Sigurdsson & Rees 1997). Stochastic scatterings with field stars will lead BHs to undergo a random walk in angular momentum, eventually pushing their pericenters inside this loss cone. If the BH is tightly bound to the MBH, the relevant loss cone is set by GW inspiral timescales and results in EMRI production; if the BH is more loosely bound, GW timescales are too long and the BH will plunge directly and unobservably into the MBH event horizon (Hopman & Alexander 2005).

EMRI rates even in this well-studied scenario are uncertain by at least three orders of magnitude (Babak et al. 2017; Broggi et al. 2022), with major systematic uncertainties stemming from the plunge-to-EMRI ratio (Qunbar & Stone 2024; Mancieri et al. 2025), the distribution of low-mass (“intermediate mass”) MBHs in dwarf galactic nuclei (Greene et al. 2020), and the ability of stellar mass BHs to replenish themselves through dynamical friction or *in situ* formation (Aharon & Perets 2016). Other EMRI formation scenarios that have been proposed more recently are even more uncertain, and include GW-driven inspirals of BHs deposited by the Hills mechanism (Miller et al. 2005; Raveh & Perets 2021); Kozai-Lidov cycles in MBH-MBH binaries (Naoz et al. 2022; Mazzolari et al. 2022); and gas-assisted inspirals in active galactic nuclei (Levin 2007; Pan et al. 2021; Derdzinski & Mayer 2023).

Given the present state of theoretical EMRI predictions, it may seem unkind to draw attention to another systematic uncertainty, but that is the purpose of this paper. A key variable strongly influencing both volumetric EMRI rates and peak GW strain is the spin,  $\chi_\bullet$ , of the primary MBH. Larger  $\chi_\bullet$  allows EMRIs to approach closer to the horizon before plunging, producing stronger signals detectable over a larger cosmological volume. More subtly,  $\chi_\bullet$  can dramatically affect the competition between GW dissipation and stochastic scattering that determines the EMRI-to-plunge ratio in loss cone channels. Amaro-Seoane et al. (2013) investigated this and found that as  $\chi_\bullet$  increases from 0 to values near 1, the EMRI rate can in principle increase by a factor of  $\approx 30$ , largely due to the enhanced GW dissipation rate for prograde, near-equatorial orbits. To the best of our knowledge, this was the last investigation of how  $\chi_\bullet$  affects loss cone dynamics for EMRIs.

In this paper, we will re-examine the role of MBH spin in setting EMRI event rates and parameters. We will go beyond the “fixed inclination” approximation of Amaro-Seoane et al. (2013) by allowing for inclination diffusion, a critical extra physical ingredient. We will also perform the first ever Monte Carlo simulations of individual BH trajectories as they diffuse through three-dimensional action space and into the horizon of the central *spinning* MBH. In §2, we take the standard formalism for stellar diffusion via two-body scatterings, normally applied to Keplerian orbits, and extend it into Kerr metric geodesics. In §3, we review and describe an analytic kludge scheme for estimating GW losses and the impact on each of the Kerr integrals of motion. In §4, we present our numerical algorithm for solving the Langevin-like equation describing orbit-averaged evolution of test BHs in Kerr spacetime. In §5, we present the results from both individual Monte Carlo simulations and large statistical ensembles of these simulations, and in §6 we summarize our main conclusions.

## 2. GEODESIC DIFFUSION COEFFICIENTS

Dense stellar environments such as galactic nuclei can be understood as weakly collisional kinetic systems. Weak, uncorrelated two-body scatterings between stars will stochastically perturb the velocity vector of a test star (or BH). By integrating over distributions of field star velocities and impact parameters, one can derive velocity-space diffusion coefficients (DCs) encapsulating this process. This statistical formalism was first pursued to study globular clusters (Spitzer & Hart 1971), but for a thorough review of stellar diffusion in galactic nuclei, see Merritt (2013). As galactic nuclei are both quasi-spherical and dominated by the gravitational field of the central MBH, stellar orbits are integrable or nearly so (ignoring for now GW dissipation), and it can be more fruitful to work with DCs in action space.

Many previous works have studied EMRI formation in the loss cone channel via these types of action-space DCs (Hopman & Alexander 2005; Bar-Or & Alexander 2016; Raveh & Perets 2021; Broggi et al. 2022; Qunbar & Stone 2024; Mancieri et al. 2025). Because orbits typically evolve only slowly<sup>2</sup>, these DCs are often orbit-averaged to simplify the problem. Orbit-averaged DCs can be used to find semi-analytic or analytic solutions to the Fokker-Planck equation (Lightman & Shapiro 1977), describing the evolution of large populations of test objects. Alternatively, they can be applied on a particle-by-particle basis to solve a Langevin-like stochastic dif-

<sup>1</sup> Equivalently, a paraboloidal region of angular momentum space.

<sup>2</sup> Though see Kaur & Perets (2024) for the role that strong scatterings can play in pre-emptively ejecting BHs before an EMRI.

ferential equation (Shapiro & Marchant 1978), as we will do in this work. Past approaches usually assume spherical symmetry (both in the gravitational potential and the distribution of field stars) so that diffusion can be studied in just two integrals of motion, orbital energy  $E$  and total angular momentum  $L$ .

In this paper we are especially concerned with the role played by inclination diffusion for geodesics in the axisymmetric Kerr metric, which has three integrals of motion:  $E$ , the  $z$ -component of angular momentum  $L_z$ , and the Carter constant  $Q$  (Bardeen et al. 1972). In this section, we therefore derive an extension to the classic 2D theory of stellar diffusion into the 3D space of Kerr geodesic integrals of motion, with the ultimate goal of producing geodesic diffusion coefficients (GDCs).

### 2.1. Approximate Theory of EMRI Formation

When a CO with mass  $m_\bullet$  orbit around a MBH with mass  $M_\bullet$  on a highly eccentric orbit with semimajor axis  $a$  and eccentricity  $e$ , two time scales are relevant for EMRIs:

- The relaxation timescale  $t_{\text{rlx}}$ - the time it takes for two-body encounters to change the orbital parameters significantly,
- The GW inspiral time  $t_{\text{GW}}$ - the time it takes GW emission to change the orbital parameters significantly.

Far from the MBH, GWs are weak and stochastic, weak two-body encounters with the other stars in the cluster dominate the evolution of the orbit. These encounters change both the energy and the angular momentum (equivalently the semimajor axis and the eccentricity), but they are typically more efficient at changing angular momentum than energy (Alexander 2017). Assuming the stellar cluster is spherically symmetric with density profile  $\rho(r) = \rho_{\text{inf}}(r/r_{\text{inf}})^{-\gamma}$ , where  $r_{\text{inf}}$  is the influence radius and  $\rho_{\text{inf}}$  is the mass density at that radius, and assuming a Keplerian potential  $\Phi = -GM_\bullet/r$  so that the local velocity dispersion is  $\sigma(r) = GM_\bullet/[r(1 + \gamma)]$ , the angular momentum relaxation time is (Hopman & Alexander 2005; Bortolas & Mapelli 2019):

$$t_{\text{rlx}} \sim \frac{L}{\dot{L}} \sim \frac{2k\sigma^3(r)}{G^2 n(r)m^2 \ln \Lambda} (1 - e) \quad (1)$$

where  $k \approx 0.34$  (Binney & Tremaine 2008),  $n(r) = \rho(r)/m$  is the stellar number density,  $\ln \Lambda \approx \ln(0.4M_\bullet/m)$  is the Coulomb logarithm, and  $m$  is the average stellar mass in the cluster.

As the CO undergoes stochastic evolution in energy and angular momentum, it can reach close enough to the

MBH, where GW emission becomes increasingly important. At each pericenter passage, the orbit loses energy and angular momentum, which causes both the semimajor axis and the eccentricity to decrease. The orbit-averaged specific energy and angular momentum losses at leading post-Newtonian order are (Peters 1964):

$$\begin{aligned} \Delta E_{\text{GW}} &= -\frac{64\pi G^{7/2} M^{5/2} m_\bullet}{5c^5 a^{7/2} (1 - e^2)^{7/2}} \left( 1 + \frac{73}{24}e^2 + \frac{37}{96}e^4 \right) \\ \Delta L_{\text{GW}} &= -\frac{64\pi G^3 M^2 m_\bullet}{5c^5 a^2 (1 - e^2)^2} \left( 1 + \frac{7}{8}e^2 \right). \end{aligned} \quad (2)$$

For a highly eccentric orbit, the GW inspiral time is (Peters 1964):

$$t_{\text{GW}} = \frac{24\sqrt{2}}{85} \frac{a^4 c^5}{G^3 M_\bullet^2 m_\bullet} (1 - e)^{7/2}. \quad (3)$$

In the picture described above, where the orbital evolution is governed either by two-body scatterings or by GW dissipation, the relative size of the two timescales determines the evolution of the CO orbit. When  $t_{\text{rlx}} < t_{\text{GW}}$ , the CO evolves stochastically and two-body scatterings dominate the changes in its orbital parameters. When  $t_{\text{GW}} < t_{\text{rlx}}$ , GWs take over and the orbit evolves deterministically, shrinking and circularizing as the CO approaches the MBH. Once  $t_{\text{GW}} \ll t_{\text{rlx}}$  an EMRI forms and the CO undergoes a slow inspiral.

However, not all orbit evolution produces long-lived GW signals. If the CO's pericenter enters the loss cone, the object plunges directly through the MBH event horizon and does not generate a detectable inspiral. Previous studies show that such plunging orbits emit only a short GW burst, detectable only for events originating in the Galactic Center (Hopman et al. 2007), and their rates are expected to be low. These orbits are therefore considered lost from the system. The boundary defining the loss cone is the innermost bound circular orbit (IBCO), corresponding to the last parabolic orbit (Bardeen et al. 1972). For a non-spinning MBH, its angular momentum is  $L_{\text{IBCO}} = 4GM_\bullet/c$ . If we are interested in estimating the EMRI to plunge ratio, this radius plays a key role.

Because  $t_{\text{GW}}$  decreases more rapidly than  $t_{\text{rlx}}$  as the CO approaches the IBCO, there exists a critical semimajor axis that separates true EMRIs from plunges (Hopman & Alexander 2005). This critical value is obtained by equating  $t_{\text{rlx}} = ft_{\text{GW}}$  and requiring that the resulting pericenter be compared with the IBCO:

$$a_c^{3-\gamma} = \frac{85\pi}{6\sqrt{2}} \frac{k f}{(1 + \gamma)^{3/2} (3 - \gamma)} \frac{G^{5/2} M_\bullet^{5/2} m_\bullet M_\odot r_{\text{inf}}^{3-\gamma}}{c^5 r_{\text{IBCO}}^{5/2} m^2 \ln \Lambda} \quad (4)$$

where  $f$  is a safety factor that ensures  $t_{\text{GW}} \ll t_{\text{rlx}}$ , and  $r_{\text{IBCO}}$  is the IBCO pericenter. This critical semimajor axis implies that an orbit starting with an initial semimajor axis below the critical value,  $a \lesssim a_c$ , will eventually reach the region where  $t_{\text{GW}} < ft_{\text{rlx}}$  before crossing the IBCO, and will therefore become an EMRI. In contrast, if the initial semimajor axis is larger than the critical value,  $a \gtrsim a_c$ , two-body scatterings always dominate and the orbit will eventually plunge into the MBH.

Previous research show that this simple EMRI–plunge dichotomy does not hold for intermediate-mass black holes (Qunbar & Stone 2024; Mancieri et al. 2025). In addition, the spin of the MBH modifies this picture and affects the resulting EMRI rates (Amaro-Seoane et al. 2013; Sun et al. 2025). The IBCO depends on both the MBH spin and the orbital inclination. For a spinning MBH, the IBCO radius decreases for prograde orbits and increases for retrograde orbits relative to the non-spinning case. This leads to a higher EMRI fraction for prograde orbits and a higher plunge fraction for retrograde ones. Consequently, instead of a single IBCO and a single corresponding critical semimajor axis, a spinning MBH yields a range of IBCOs that define a range of critical semimajor axes.

To estimate how the MBH spin, and therefore the orbital inclination, affect the EMRI rates, Amaro-Seoane et al. (2013) define the ratio between the IBCO radii in the Kerr and the Schwarzschild cases:

$$\mathcal{W}(\chi_\bullet, \iota) \equiv \frac{r_{\text{IBCO}, \text{Kerr}}}{r_{\text{IBCO}, \text{Schw}}}.$$
 (5)

Using this ratio, they calculated the corresponding change in the EMRI rate:

$$\dot{N}_{\text{EMRI}}^{\text{Kerr}} = \dot{N}_{\text{EMRI}}^{\text{Schw}} \mathcal{W}^{\frac{20\gamma-45}{12-4\gamma}}(\chi_\bullet, \iota)$$
 (6)

As an example, they showed that for a spin of  $\chi_\bullet = 0.999$  and an inclination of  $\iota = 0.4$  rad, the EMRI rate increases significantly, with  $\dot{N}_{\text{EMRI}}^{\text{Kerr}} \sim 30 \dot{N}_{\text{EMRI}}^{\text{Schw}}$ . This is an enhancement by a factor of about 30 relative to the non-rotating case.

However, this estimate assumes that the inclination remains fixed during the evolution. In reality, two-body scatterings also modify the inclination. To investigate inclination diffusion and its impact on EMRI rates when the MBH is spinning, we need to extend the classical 2D Newtonian theory of stellar diffusion coefficients into the full 3D Kerr spacetime along geodesic motion. This mathematical framework is developed in the next section.

## 2.2. Local Diffusion Coefficients

To describe the effect of weak gravitational encounters, we use the Fokker–Planck equation. It describes the change in the distribution function produced by collisions,  $\left(\frac{\partial f_b}{\partial t}\right)_c$ , where  $f_b(t, \vec{x}, \vec{v})$  is the phase-space number density of field stars of mass  $m_b$ , depending on time  $t$ , position  $\vec{x}$ , and velocity  $\vec{v}$ . The Fokker–Planck equation describes the time evolution of  $f_b$  as

$$\left(\frac{\partial f_b}{\partial t}\right)_c = -\frac{\partial}{\partial v^i} (f_b \langle \Delta v^i \rangle) + \frac{1}{2} \frac{\partial^2}{\partial v^i \partial v^j} (f_b \langle \Delta v^i \Delta v^j \rangle) \quad (7)$$

where  $v^i$  ( $i = 1, 2, 3$ ) is the  $i$ th component of velocity in Cartesian coordinates and  $\langle \Delta v^i \rangle$  is the average change in  $v^i$  per unit time experienced by a test star through interactions with all other stars in the cluster. In this section, we adopt the Einstein summation convention.

The derivation of the Fokker–Planck equation assumes that only distant encounters are relevant, so that changes in  $v^i$  are small. Accordingly, only the first-order  $\langle \Delta v^i \rangle$  and second-order  $\langle \Delta v^i \Delta v^j \rangle$  diffusion coefficients are considered. The diffusion coefficients for a test object of mass  $m$ , are given by

$$\begin{aligned} \langle \Delta v^i \rangle &= \Gamma' \sum_b m_b (m + m_b) \frac{\partial h_b}{\partial v^i}, \\ \langle \Delta v^i \Delta v^j \rangle &= \Gamma' \sum_b m_b^2 \frac{\partial^2 g_b}{\partial v^i \partial v^j}, \\ h_b(\vec{v}) &\equiv \int \frac{f_b(\vec{v}_f)}{|\vec{v} - \vec{v}_f|} d\vec{v}_f \\ g_b(\vec{v}) &\equiv \int f_b(\vec{v}_f) |\vec{v} - \vec{v}_f| d\vec{v}_f \end{aligned} \quad (8)$$

where  $\Gamma' \equiv 4\pi G^2 \ln \Lambda$ ,  $G$  is the gravitational constant, and  $\ln \Lambda$  is the Coulomb logarithm. The sums over  $b$  run over all stellar species in the system, each with mass  $m_b$  and distribution function  $f_b$ .

However, the diffusion coefficients above are expressed in Cartesian velocity components, whereas our goal is to work in terms of the constants of motion of the system. In the Kerr metric, there are three such constants: the energy  $E$ , the  $z$ -component of the angular momentum  $L_z$  and the Carter constant  $Q$ . In Boyer-Lindquist coordinates  $(r, \theta, \phi)$ , which reduce to spherical coordinates far from the black hole, the specific values of these constants can be written as

$$E = c^2 + \frac{v^2}{2} + \Phi(\vec{x}) \quad (9a)$$

$$L_z = r \sin \theta v_\phi \quad (9b)$$

$$Q = r^2 v_\theta^2 + \cos^2 \theta [x_\bullet^2 (1 - E^2/c^4) + L_z^2/\sin^2 \theta] \quad (9c)$$

where  $0 \leq \chi_\bullet \leq \frac{GM_\bullet}{c}$  is the spin of the MBH with mass  $M_\bullet$ , and  $\Phi(r)$  is the stellar potential.

In Appendix A, we derive the local diffusion coefficients for the three constants of motion in Eq. (9) for a general, non-spherical field of stars. The general expressions are given in Eqs. (A10) and (A11). While these expressions apply to arbitrary velocity distributions, in this paper we focus on the simpler case of a potential which depends only on the radial coordinate  $r$ ,  $\Phi(r)$  (i.e., one which asymptotes to spherical symmetry far from the black hole), and with an isotropic field-star velocity distribution. In such a system,  $h_b$  and  $g_b$  depend only on  $v$ , which significantly simplifies the diffusion coefficients. In velocity space, the only non-zero diffusion coefficients up to second order are:

$$\begin{aligned} \langle \Delta v_{\parallel} \rangle &= \Gamma' \sum_b m_b (m + m_b) \frac{dh_b}{dv}, \\ \langle (\Delta v_{\parallel})^2 \rangle &= \Gamma' \sum_b m_b^2 \frac{d^2 g_b}{dv^2}, \\ \langle (\Delta v_{\perp})^2 \rangle &= \frac{2\Gamma'}{v} \sum_b m_b^2 \frac{dg_b}{dv} \end{aligned} \quad (10)$$

where  $v_{\parallel}$  is the velocity component parallel to the motion of the test object, and  $v_{\perp}$  is the component perpendicular to it. In the isotropic limit,  $h_b$  and  $g_b$  reduce to:

$$\begin{aligned} h_b(v) &= 4\pi v [I_2(v) + J_1(v)], \\ g_b(v) &= \frac{4\pi v^3}{3} [3I_2(v) + I_4(v) + 3J_3(v) + J_1(v)], \\ I_n(v) &= \int_0^v \left(\frac{v_f}{v}\right)^n f_b(v_f) dv_f, \\ J_n(v) &= \int_v^\infty \left(\frac{v_f}{v}\right)^n f_b(v_f) dv_f. \end{aligned} \quad (11)$$

Additionally, two-body scattering is most effective near the apocenter, far from the MBH, where the influence of the spin  $\chi_{\bullet}$  is negligible. Consequently, spin-dependent terms can be omitted from the coefficients. With these simplifications, the local diffusion coefficients

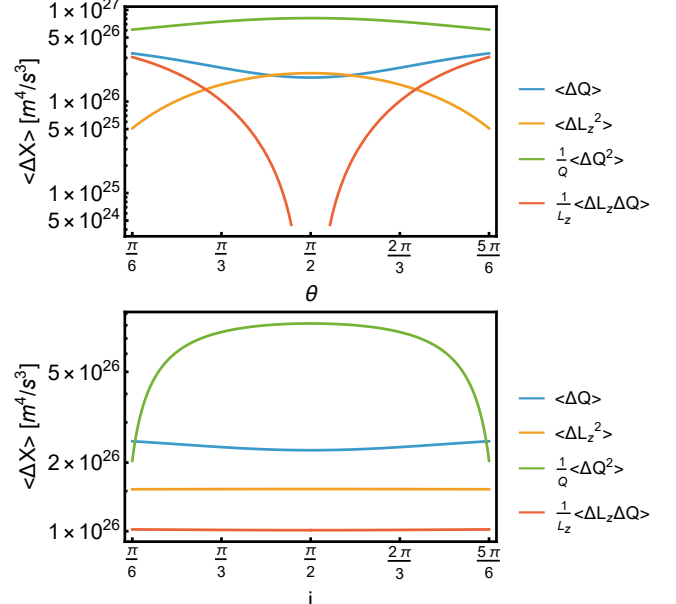


**Figure 1.** A comparison of local diffusion coefficients (excluding those derived in previous work) as a function of colatitude  $\theta$  with  $I = 60^\circ$  (top), or inclination with  $\theta = 60^\circ$  (bottom). The semimajor=  $10^7 r_g$ , eccentricity= 0.99,  $r = r_a$ ,  $M_{\bullet} = 10^6 M_{\odot}$  and  $m_{\bullet} = 10 M_{\odot}$ .

reduce to:

$$\begin{aligned}
\langle \Delta E \rangle &= \Gamma' \left[ v \frac{\partial \mathcal{H}}{\partial v} + \frac{1}{2} \frac{\partial^2 \mathcal{G}}{\partial v^2} + \frac{1}{v} \frac{\partial \mathcal{G}}{\partial v} \right] \\
&= v \langle \Delta v_{\parallel} \rangle + \frac{1}{2} \langle (\Delta v_{\parallel})^2 \rangle + \frac{1}{2} \langle (\Delta v_{\perp})^2 \rangle, \\
\langle (\Delta E)^2 \rangle &= \Gamma' \left[ v^2 \frac{\partial^2 \mathcal{G}}{\partial v^2} \right] = v^2 \langle (\Delta v_{\parallel})^2 \rangle, \\
\langle \Delta L_z \rangle &= \Gamma' \left[ \frac{L_z}{v} \frac{\partial \mathcal{H}}{\partial v} \right] = \frac{L_z}{v} \langle \Delta v_{\parallel} \rangle, \\
\langle (\Delta L_z)^2 \rangle &= \Gamma' \left[ \left( \frac{L_z}{v} \right)^2 \frac{\partial^2 \mathcal{G}}{\partial v^2} + \frac{r^2 \sin^2 \theta v^2 - L_z^2}{v^3} \frac{\partial \mathcal{G}}{\partial v} \right] \\
&= \left( \frac{L_z}{v} \right)^2 \langle (\Delta v_{\parallel})^2 \rangle + \frac{r^2 v^2 \sin^2 \theta - L_z^2}{2v^2} \langle (\Delta v_{\perp})^2 \rangle, \\
\langle \Delta Q \rangle &= \Gamma' \left[ \frac{2Q}{v} \frac{\partial \mathcal{H}}{\partial v} + \frac{Q}{v^2} \frac{\partial^2 \mathcal{G}}{\partial v^2} \right. \\
&\quad \left. + \frac{1}{v^3} (r^2 v^2 (1 + \cos^2 \theta) - Q) \frac{\partial \mathcal{G}}{\partial v} \right] \\
&= \frac{2Q}{v} \langle \Delta v_{\parallel} \rangle + \frac{Q}{v^2} \langle (\Delta v_{\parallel})^2 \rangle \\
&\quad + \frac{1}{2v^2} (r^2 v^2 (1 + \cos^2 \theta) - Q) \langle (\Delta v_{\perp})^2 \rangle, \\
\langle (\Delta Q)^2 \rangle &= \Gamma' \left\{ \frac{4Q^2}{v^2} \frac{\partial^2 \mathcal{G}}{\partial v^2} \right. \\
&\quad \left. + \left[ \frac{4r^2}{v} (Q - L_z^2 \cos^2 \theta) - \frac{4Q^2}{v^3} \right] \frac{\partial \mathcal{G}}{\partial v} \right\} \\
&= \frac{4Q^2}{v^2} \langle (\Delta v_{\parallel})^2 \rangle \\
&\quad + \left[ 2r^2 (Q - L_z^2 \cos^2 \theta) - \frac{2Q^2}{v^2} \right] \langle (\Delta v_{\perp})^2 \rangle,
\end{aligned} \tag{12}$$

and the cross terms:

$$\begin{aligned}
\langle \Delta E \Delta L_z \rangle &= \Gamma' \left[ L_z \frac{\partial^2 \mathcal{G}}{\partial v^2} \right] = L_z \langle (\Delta v_{\parallel})^2 \rangle, \\
\langle \Delta E \Delta Q \rangle &= \Gamma' \left[ 2Q \frac{\partial^2 \mathcal{G}}{\partial v^2} \right] = 2Q \langle (\Delta v_{\parallel})^2 \rangle, \\
\langle \Delta L_z \Delta Q \rangle &= \Gamma' \left[ \frac{2L_z Q}{v^2} \frac{\partial^2 \mathcal{G}}{\partial v^2} \right. \\
&\quad \left. - \frac{2L_z}{v^3} (Q - r^2 v^2 \cos^2 \theta) \frac{\partial \mathcal{G}}{\partial v} \right] \\
&= \frac{2L_z Q}{v^2} \langle (\Delta v_{\parallel})^2 \rangle \\
&\quad - \frac{L_z}{v^2} (Q - r^2 v^2 \cos^2 \theta) \langle (\Delta v_{\perp})^2 \rangle.
\end{aligned} \tag{13}$$

We first note that the energy diffusion coefficients  $\langle \Delta E \rangle$  and  $\langle (\Delta E)^2 \rangle$  obtained for a spherical and isotropic stellar field are identical to those in the standard 2D case. Also, our new local diffusion coefficients in 3D,

$\langle \Delta Q \rangle$  and  $\langle \Delta L_z \rangle$ , can be directly related to the 2D coefficient  $\langle \Delta L \rangle$  by noting that in Kerr spacetime, in the limit  $\chi_{\bullet} = 0$ , the constants of motion satisfy  $Q + L_z^2 = L^2$ . This implies that  $\langle \Delta Q \rangle + \langle (\Delta L_z)^2 \rangle = \langle (\Delta L^2) \rangle$  where all quantities in angle brackets denote *first* order diffusion coefficients. A similar relation holds for the second order terms. Moreover, the relation between  $\langle \Delta (L^2) \rangle$  and  $\langle \Delta L \rangle$  can be calculated analytically:

$$\langle \Delta (L^2) \rangle = 2L \langle \Delta L \rangle + \langle (\Delta L)^2 \rangle \tag{14}$$

where the last term on the right hand side is a second order diffusion coefficient. This expression is also valid when replacing  $L$  with  $L_z$ . Therefore, the 3D diffusion formalism naturally reduces to the 2D case in the limit  $\chi_{\bullet} = 0$  using:

$$\langle \Delta Q \rangle + 2L_z \langle \Delta L_z \rangle + \langle (\Delta L_z)^2 \rangle = 2L \langle \Delta L \rangle + \langle (\Delta L)^2 \rangle. \tag{15}$$

The new local diffusion coefficients depend not only on  $r$  but also on  $\theta$ . In addition, because we derived the coefficients in three dimensions, they also depend on the orbital inclination. In this paper we use two definitions of the inclination, which are equivalent in the Schwarzschild limit:

$$\begin{aligned}
Q &= L_z^2 \tan^2 I + \chi_{\bullet}^2 (1 - E^2) \sin^2 I \\
Q &= L_z^2 \tan^2 \iota.
\end{aligned} \tag{16}$$

Fig. 1 shows the dependence of the local diffusion coefficients on both  $\theta$  and the inclination.

### 2.3. Torus-Averaged Diffusion Coefficients

To simplify the problem further, we assume that the timescale for changes in  $f_b$  due to collisions is long compared with the orbital period. Under this assumption, the local diffusion coefficients can be replaced by their time averages over many orbits. Because the diffusion coefficients in Eqs. (12) and (13) depend explicitly on  $r$  and  $\theta$ , averaging requires integration over both coordinates. The full derivation is presented in Appendix B. The orbit-averaged value of a general diffusion coefficient  $\langle \Delta V^i \rangle$  where  $V^i \in \{E, L_z, Q\}$  is given by

$$\begin{aligned}
\langle \Delta V^i \rangle_o &\equiv \frac{\int_{\theta_{\min}}^{\theta_{\max}} \int_{r_p}^{r_a} J \langle \Delta V^i \rangle dr d\theta}{\int_{\theta_{\min}}^{\theta_{\max}} \int_{r_p}^{r_a} J dr d\theta}, \\
J &\equiv \frac{\Sigma(r, \theta)^2}{r^2 \sqrt{R(r)} \sqrt{\Theta(\theta)}}
\end{aligned} \tag{17}$$

where the squared velocity is  $v^2 = \dot{r}^2 + (r\dot{\theta})^2 + (r \sin(\theta)\dot{\phi})^2$ . Here, the derivatives are taken with respect to the proper time, and  $\dot{r}, \dot{\theta}, \dot{\phi}$  are the geodesic velocities as defined in Bardeen et al. (1972). The functions  $R(r)$

and  $\Theta(\theta)$  are the radial and polar potentials of the Kerr metric, and  $\Sigma = r^2 + \chi_\bullet^2 \cos^2 \theta$ .  $r_p$  and  $r_a$  are the pericenter and apocenter, respectively.  $\theta_{\min} = \pm(\pi/2 - I)$  and  $\theta_{\max} = \pi - \theta_{\min}$  are the minimum and maximum values of  $\theta$  along the orbit for a given inclination  $I$ , where the upper sign refers to prograde orbits, while the lower sign refers to retrograde orbits. These turning points are the roots of the associated radial and polar effective potentials.

### 3. GRAVITATIONAL WAVE LOSSES

When the CO reaches pericenter it loses energy and angular momentum through GW emission. Detecting EMRIs with LISA will require highly accurate theoretical models of their waveforms. However, computing EMRI waveforms is extremely challenging and is an active area of research. The difficulty arises from the need to calculate the orbital motion of the CO in the Kerr spacetime while accounting for radiation reaction. Because of the extreme mass ratio between the test object and the MBH,  $m/M_\bullet \ll 1$ , the system can be modeled using BH perturbation theory by the Teukolsky equation (Teukolsky 1973). However, generating waveforms by solving the Teukolsky equation is computationally expensive. Consequently, for LISA data analysis or for astrophysical estimates such as those considered in this work, approximate waveform models have been developed that capture the main features of the signal (Glampedakis et al. 2002; Gair & Glampedakis 2006; Babak et al. 2007).

In this paper, we use the approach in Gair & Glampedakis (2006), which assumes that the orbital parameters evolve adiabatically. Due to the extreme mass ratio, the orbital parameters change on a timescale much longer than the orbital period. Therefore, on short timescales the motion can be approximated as geodesic, neglecting the influence of gravitational back-reaction. Within this scheme, the orbital motion is described by exact Kerr geodesic, and the orbit-averaged fluxes of the constants of motion ( $\Delta E_{\text{GW}}$ ,  $\Delta L_{z,\text{GW}}$ ,  $\Delta Q_{\text{GW}}$ ) are computed using the post-Newtonian approximation. These fluxes are then used to update the geodesic parameters, generating a new geodesic. This procedure is iterated, thereby combining an exact description of the short-timescale dynamics with an approximate treatment of long-timescale radiation reaction. For this reason, this method is commonly referred to as a “hybrid” or “kludge” approach.

In Appendix C, we show some examples of orbital evolution driven by GW emission, following Gair & Glampedakis (2006). Additionally, we compare the evo-

lution of the semimajor axis and eccentricity due to GW emission, as given in Gair & Glampedakis (2006), with the analytical expression of the Peters’ formula (Peters 1964), which is exact for circular orbits and widely used in many studies due to its simplicity. An important point in the context of this work is that the orbital inclination does not evolve significantly under GW losses. Therefore, any change in inclination is expected to arise primarily from two-body relaxation.

Since the method of Gair & Glampedakis (2006) is approximate, we test its accuracy by comparing it with results obtained using a Teukolsky-based approach. To this end, we employ the code described in (Drasco & Hughes 2006; Hughes et al. 2021), which uses black hole perturbation theory to compute the GW fluxes produced by test particles on bound geodesic orbits around rotating MBHs. The relative errors between the two approaches are shown in Fig. 2. The comparison is performed for the energy, the angular momentum in the z-direction, and the Carter constant fluxes, as functions of the pericenter radius, orbital eccentricity, inclination, and MBH spin. We find that the relative error remains below 50% as long as the pericenter radius  $r_p \gtrsim 3r_g$ .

Since Gair & Glampedakis (2006) is an approximated method, we test its accuracy compared to the Teukolsky-based results. For this aim, we used the code described in (Drasco & Hughes 2006; Hughes et al. 2021) that uses black hole perturbation theory to calculate the gravitational waves produced by test particles moving on bound geodesic orbits about rotating MBHs. The relative errors between these two approaches are shown in Fig. 2. The comparisons are presented for the fluxes in energy, angular momentum in the z-direction, and the Carter constant, as a function of the pericenter radius, the eccentricity, the orbital inclination and the MBH spin. For this comparison, we use high values of eccentricity and MBH spins, where we think Gair & Glampedakis (2006) will do the worse. We can see in Fig. 2, that the relative error is less than 50% as long as the pericenter radius  $r_p \gtrsim 3r_g$ .

### 4. MONTE CARLO ALGORITHM

To study the effect of inclination diffusion on a test CO in the nuclear cluster, we perform orbit-averaged Monte Carlo (MC) simulations. The simulations include both the stochastic perturbations from two-body relaxation with other stars in the cluster and the deterministic losses due to GW emission. We neglect scalar resonant relaxation (Rauch & Tremaine 1996), as previous studies have shown it to be relatively unimportant for EMRI rates (Bar-Or & Alexander 2016). We also neglect vector resonant relaxation (Rauch & Tremaine 1996), which

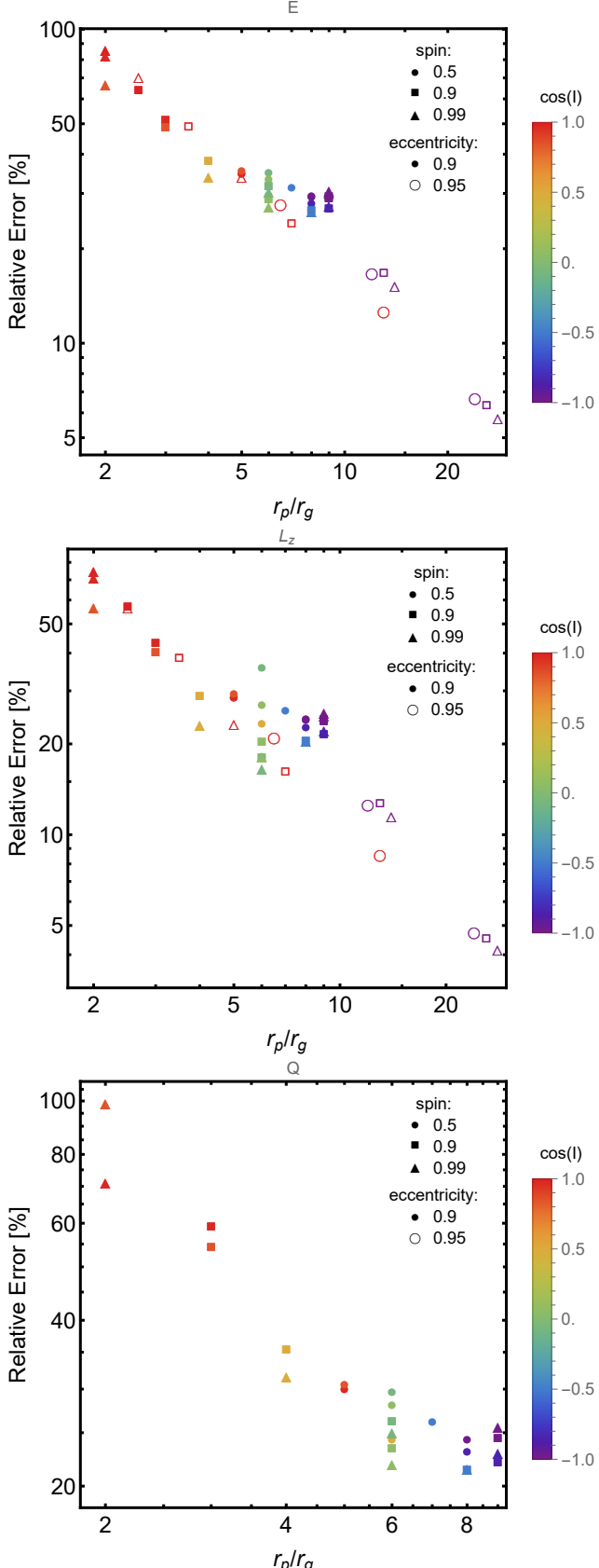


**Figure 2.** The relative error in the energy (top), angular momentum in the z-direction (middle), and the Carter constant (bottom) fluxes between the approximated GW approach (Gair & Glampedakis 2006) and the Teukolsky-based solution (Teukolsky 1973), shown as a function of pericenter distance, for different MBH spins, eccentricities and inclinations.

has not previously been studied in this context; its effect on EMRI rates in the Kerr spacetime may potentially be more important.

To capture the inclination evolution of the test CO, we evolve the three integrals of motion: the orbital energy  $E$ , the  $z$ -component of the angular momentum  $L_z$ , and the Carter constant  $Q$ . For the MC simulations, we adopt the prescription of Shapiro & Marchant (1978) with variable time steps. At each iteration, the updates to the integrals of motion are given by:

$$\begin{aligned}\delta E &= NP\Delta E_{\text{GW}} + NP\langle(\Delta E)^2\rangle_o + (NP\langle(\Delta E)^2\rangle_o)^{1/2}y_1, \\ \delta L_z &= NP\Delta L_{z,\text{GW}} + NP\langle(\Delta L_z)^2\rangle_o + (NP\langle(\Delta L_z)^2\rangle_o)^{1/2}y_2, \\ \delta Q &= NP\Delta Q_{\text{GW}} + NP\langle(\Delta Q)^2\rangle_o + (NP\langle(\Delta Q)^2\rangle_o)^{1/2}y_3\end{aligned}\quad (18)$$

where each iteration corresponds to  $N$  orbits with orbital period  $P$ . The value of  $NP$  is determined such that the change in each integral at a given iteration remains a small fraction of its value from the previous step, while never being shorter than a single orbital period.  $\Delta X_{\text{GW}}$  are the changes due to GW emission (§3), as in Gair & Glampedakis (2006),  $\langle(\Delta X)\rangle_o$  are the orbit-averaged diffusion coefficients from §2, and  $y_i$  are random variables drawn from a 3D multivariate Gaussian distribution with mean  $\langle y_i \rangle = 0$  and variance-covariance matrix:

$$\begin{bmatrix} 1 & \frac{\langle\Delta E\Delta L_z\rangle_o}{\sqrt{\langle(\Delta E)^2\rangle_o\langle(\Delta L_z)^2\rangle_o}} & \frac{\langle\Delta E\Delta Q\rangle_o}{\sqrt{\langle(\Delta E)^2\rangle_o\langle(\Delta Q)^2\rangle_o}} \\ \frac{\langle\Delta E\Delta L_z\rangle_o}{\sqrt{\langle(\Delta E)^2\rangle_o\langle(\Delta L_z)^2\rangle_o}} & 1 & \frac{\langle\Delta L_z\Delta Q\rangle_o}{\sqrt{\langle(\Delta L_z)^2\rangle_o\langle(\Delta Q)^2\rangle_o}} \\ \frac{\langle\Delta E\Delta Q\rangle_o}{\sqrt{\langle(\Delta E)^2\rangle_o\langle(\Delta Q)^2\rangle_o}} & \frac{\langle\Delta L_z\Delta Q\rangle_o}{\sqrt{\langle(\Delta L_z)^2\rangle_o\langle(\Delta Q)^2\rangle_o}} & 1 \end{bmatrix}. \quad (19)$$

In this work, we assume a single-mass stellar population with  $m_b = 1M_\odot$ , an isotropic velocity distribution, and a power-law mass density profile  $\rho(r) = \rho_{\text{inf}}(r/r_{\text{inf}})^{-\gamma}$  where  $r_{\text{inf}}$  is the influence radius and  $\rho_{\text{inf}}$  is the mass density at  $r_{\text{inf}}$ . The influence radius is defined as the radius enclosing twice the black hole mass, and can also be expressed as  $r_{\text{inf}} = GM_\bullet/\sigma^2$ , where  $\sigma$  is the stellar velocity dispersion in the galactic center. In this work, we use the  $\sigma$  from the  $M - \sigma$  relation,  $\sigma = 70(M_\bullet/1.53 \times 10^6 M_\odot)^{1/4.24}$  km/s (Gültekin et al. 2009). The gravitational potential is assumed to be  $\Phi(r) = -GM_\bullet/r$ , and using Eddington's integral, the number density is

$$f(E) = \frac{3-\gamma}{8} \sqrt{\frac{2}{\pi^5}} \frac{\Gamma(\gamma+1)}{\Gamma(\gamma-\frac{1}{2})} \frac{M_\bullet}{m_\star} \frac{\phi_0^{3/2}}{(GM_\bullet)^3} \left(\frac{|E|}{\phi_0}\right)^{\gamma-3/2} \quad (20)$$

where  $\phi_0 = GM_\bullet/r_{\text{inf}}$ . For the density slope, we use the Bahcall–Wolf value  $\gamma = 7/4$ . The use of a Keplerian potential limits us to consider the stellar distribution

only at radii  $R_g \ll r \ll r_{\text{inf}}$ . At radii  $r \sim R_g$ , Eq. 20 will be inconsistent, but this matters little because here we are well inside the radii where stellar scatterings matter. At radii  $r \gtrsim r_{\text{inf}}$ , our neglect of the stellar potential will invalidate both Eq. 20 as well as our torus-averaging procedure, so this limits the radial range over which can consider EMRI formation.

The simulation is terminated when the test CO either crosses the IBSO and undergoes a direct plunge, or when it satisfies the condition  $t_{\text{GW}} = 10^{-3} t_{\text{rlx}}$  (Hopman & Alexander 2005), indicating that it has entered deep into the GW-dominated regime and will become an EMRI. An additional termination condition is applied when the CO reaches a large semimajor axis ( $a > r_{\text{inf}}/3$ ), in which case the simulation is stopped and rerun.

## 5. RESULTS

In this section, we present the results of our MC simulation investigating the effect of inclination diffusion. Previous study defined a critical semimajor axis separating EMRIs from plunges (Hopman & Alexander 2005). However, since the IBSO depends on inclination, adding the inclination diffusion transforms this critical value into a range of semimajor axes. This range is shown in Fig. 3, and it marks the region where inclination diffusion has the strongest impact on the EMRI-to-plunge ratio.

Two example runs from our MC code are presented in Figs. 3 and 4. The simulations are initialized with semimajor axes, eccentricities, and inclinations of  $(10^5 r_g, 0.99, 60^\circ)$  and  $(10^6 r_g, 0.9, 60^\circ)$ . In the first case, the orbit crosses the IBSO and results in a plunge, while in the second it enters the region where GW emission dominates over two-body scattering, leading to an EMRI. In both runs, the inclination diffuses due to two-body scatterings, which can flip the orbit from prograde to retrograde. Once the CO enters the GW-dominated regime, however, inclination diffusion halts.

To systematically investigate this, we ran a large number of the MC simulations for a range of initial semimajor axes. In all runs, the initial eccentricity was fixed at  $e_{\text{init}} = 0.999$ , while the initial inclination was randomly sampled from a uniform distribution. Following Hopman & Alexander (2005), we estimate the EMRI-to-plunge ratio using the “S-curves”, defined as

$$S(a_{\text{init}}) = \frac{N_{\text{EMRI}}}{N_{\text{EMRI}} + N_{\text{plunge}}} \quad (21)$$

where  $N_{\text{EMRI}}$  and  $N_{\text{plunge}}$  are the number of EMRIs and plunges, respectively, for a given initial semimajor axis  $a_{\text{init}}$ .

In Fig. 5, we show the S-curves for the 2D and 3D cases for an MBH with mass  $M_\bullet = 10^6 M_\odot$ , and three

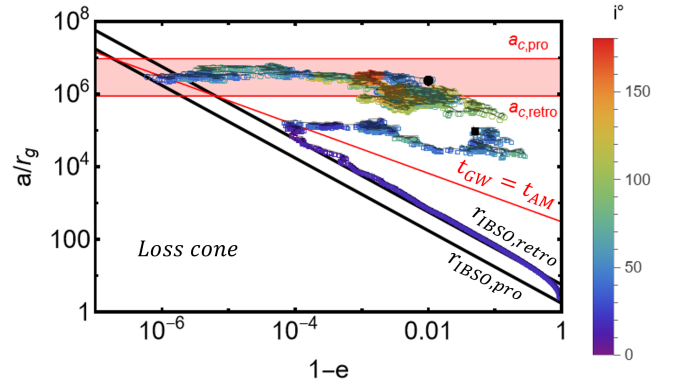


**Figure 3.** Two examples of random walks from the 3D Monte Carlo simulation: one is a plunge orbit (starting at the circle point) and one is an EMRI (starting at the square point). The trajectories are shown as semimajor axis versus the inverse eccentricity, with colors indicating the inclination. The spin of the MBH is  $\chi_\bullet = 0.9$ , its mass is  $M_\bullet = 10^6 M_\odot$ , and the mass of the CO is  $m_\bullet = 10 M_\odot$ . The solid lines are the IBSOs for equatorial prograde and retrograde orbits. The red curve indicates where the GW timescale equals the relaxation time; this defines a critical range of semimajor axes, highlighted in the red region. The figure shows that the inclination can evolve due to two-body scatterings.

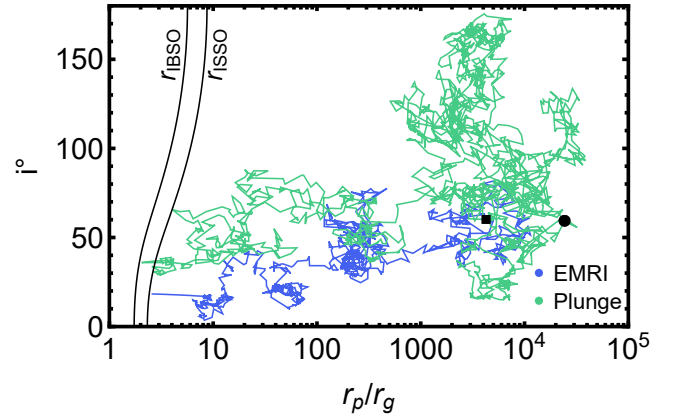


**Figure 4.** Same runs as in Fig. 3, now shown as inclination as a function of pericenter. The black curves are the IBSO and the ISSO, plotted for the plunge and EMRI orbits at their final inclination, respectively.

CO masses  $m_\bullet \in \{1.4 M_\odot, 10 M_\odot, 50 M_\odot\}$ . In the 2D case, only  $E$  and  $L$  are evolved, while in the 3D case  $E$ ,  $L_z$ , and  $Q$  are evolved to include inclination diffusion. To isolate the effect of evolving on Keplerian orbits versus geodesics, we present 2D results using both Keplerian trajectories and geodesics, with gravitational wave fluxes computed using the formalism of Peters (1964). In the 3D case, the motion is along geodesics and the GW fluxes follow Gair & Glampedakis (2006). For the 3D results, we show both a non spinning MBH

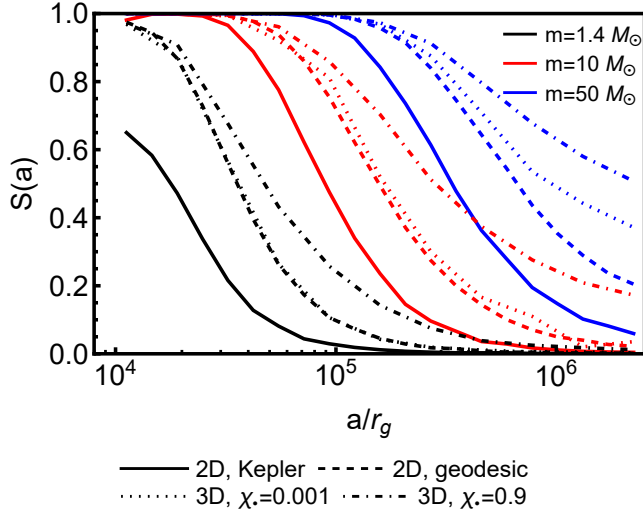


**Figure 5.** The EMRI fractions from all the captures in the simulations as a function of the initial semimajor axis (the s-curves defined in Eq. 21). We compare the 2D and 3D cases. Solid lines show the 2D case on Keplerian trajectories, and dashed lines show the 2D case on geodesics. In both cases, GW fluxes follow Peters (1964). Dotted and dot dashed lines show the 3D cases, evolved on geodesics with GW fluxes from Gair & Glampedakis (2006), for a non-spinning MBH ( $\chi_\bullet = 0.001$ ) and a highly spinning MBH ( $\chi_\bullet = 0.9$ ), respectively. The MBH mass is  $M_\bullet = 10^6 M_\odot$ , and the CO masses are:  $m_\bullet = 1.4 M_\odot$  (black),  $m_\bullet = 10 M_\odot$  (red), and  $m_\bullet = 50 M_\odot$  (blue). Geodesic orbits yield more EMRIs than Keplerian orbits, and spinning MBHs yield more EMRIs than non-spinning MBHs.

case ( $\chi_\bullet = 0.001$ ) and a highly spinning MBH case ( $\chi_\bullet = 0.9$ ).

We first note a clear difference between the 2D cases evolved on Keplerian orbits and those evolved on geodesics. Naively, one might expect little to no difference between these approaches, but as suggested by Mancieri et al. (2025), including Post-Newtonian corrections increases the number of EMRIs. We also find that the 3D non-spinning case is very similar to the 2D case evolved on geodesic orbits. This indicates that the discrepancy originates from evolving the orbit along a geodesic rather than a Keplerian trajectory, and not from the choice between 2D and 3D evolution or from using Peters (1964) versus Gair & Glampedakis (2006). On geodesics, GW emission is stronger while the diffusion coefficients are weaker, which leads to an increased number of EMRIs. Finally, we compare the non-spinning case with a rapidly spinning MBH, including the effects of inclination diffusion, and find from Fig. 5 that increasing the MBH spin leads to a higher number of EMRIs.

## 6. CONCLUSIONS

Estimates of EMRI rates remain highly uncertain, even for the most extensively studied formation channel, the loss cone (Babak et al. 2017). One source of this uncertainty is the spin of the MBH, as observational evidence indicates that a substantial fraction of MBHs in the Universe are rapidly rotating (Reynolds 2021). The MBH spin can significantly influence the EMRI-to-plunge ratio, since the IBCO, which is the limit radius for the last parabolic orbit, depends sensitively on the spin magnitude. For rapidly spinning MBHs, the IBCO decreases for prograde orbits, allowing COs to approach the MBH more closely without plunging and thereby increasing the EMRI formation rate. In contrast, for retrograde orbits, the IBCO increases, leading to an enhanced rate of direct plunges. Previous studies have demonstrated that highly spinning MBHs combined with low-inclination CO orbits can substantially increase the EMRI fraction (Amaro-Seoane et al. 2013); however, these estimates assumed a fixed orbital inclination throughout the orbital evolution.

However, two-body scatterings not only alter the energy and angular momentum of the CO but also modify its orbital inclination. Because the IBCO, and consequently the EMRI-to-plunge ratio, is sensitive to inclination in the presence of MBH spin, inclination evolution must be incorporated into accurate EMRI rate estimates. To this end, we developed the mathematical framework required to describe inclination diffusion driven by two-body encounters. Specifically, we generalize the conventional two-dimensional diffusion-coefficient formalism to three dimensions by evolving the three constants of motion in the Kerr spacetime: the energy,  $E$ , the angular momentum component in the  $z$ -direction,  $L_z$ , and the Carter constant,  $Q$  (Bardeen et al. 1972), rather than the energy,  $E$ , and the total angular momentum,  $L$ , alone.

Another key ingredient in EMRI formation is GW emission. Because computing the evolution of CO orbits in Kerr spacetime by solving the Teukolsky equation is computationally expensive, we adopted an approximate approach following Gair & Glampedakis (2006). This method assumes that the evolution of the orbital parameters occurs on timescales much longer than the orbital period. Accordingly, the CO is taken to move along a sequence of geodesics, where the back-reaction is neglected on orbital timescales, and the constants of motion are updated iteratively using orbit-averaged GW fluxes computed within the post-Newtonian approximation.

To investigate the impact of inclination diffusion in the presence of MBH spin, we incorporate the newly derived diffusion coefficients together with the GW scheme into

MC simulations. We find that the orbital inclination of the CO can evolve substantially over the course of the simulation, with initially prograde orbits becoming retrograde and vice versa, demonstrating that the fixed-inclination assumption is inaccurate. To quantify the effect on EMRI formation, we systematically compute the s-curves, defined as the fraction of EMRIs over the total number of captures. We compared three cases: a 2D formulation assuming Keplerian orbits, a 2D formulation following geodesic motion, and a 3D formulation with geodesic motion, all for a nonspinning MBH. We find that geodesic motion yields a higher EMRI fraction than the Keplerian approximation, indicating that future EMRI rate estimates must account for relativistic orbital dynamics rather than relying on Keplerian orbits. Finally, we compute the s-curves for spinning MBHs using the 3D diffusion coefficients and find that rapid MBH spin further enhances the EMRI fraction.

In this work, we improved the treatment of orbital inclination evolution driven by two-body scatterings; however, several additional dynamical processes operating in galactic nuclei were neglected. Previous studies have shown that scalar resonant relaxation is relatively unimportant for EMRI formation (Bar-Or & Alexander 2016). In contrast, vector resonant relaxation (Rauch & Tremaine 1996), which can significantly modify the inclination distribution of COs in the cluster, has not yet been explored in the context of EMRI rate estimates. We also neglect the gravitational potential of the surrounding stellar cluster and assume a spherical potential from the MBH. Deviations from spherical symmetry, such as axisymmetric or triaxial potentials, can induce anisotropic two-body scatterings that may alter our results (Vasiliev & Merritt 2013; Kaur & Stone 2025). Furthermore, our simulations model scatterings with stars following a Bahcall-Wolf distri-

bution. Using a more strongly mass-segregated distribution function could change the abundance of stellar-mass BHs and therefore the EMRI rates (Hopman & Alexander 2006; Broggi et al. 2024; Rom et al. 2024). Moreover, in the case of spinning MBHs, the presence of an ergosphere allows plunging COs to remain near the MBH for extended periods before crossing the event horizon, potentially producing EMRI-like GW signals (Schnittman 2015; Naoz et al. 2022). Finally, the approximate gravitational-wave emission scheme employed in this work (Gair & Glampedakis 2006) can differ from Teukolsky-based calculations by tens of percent. Adopting a more accurate treatment may modify our results.

The EMRI rate remain highly uncertain, and in this project we focus on another systematic uncertain, the role of inclination diffusion when the MBH is spinning. In this project, we addressed only the loss cone formation channel, but our new mathematical framework to two-body scatterings in 3D can also be relevant to other formation channels such as wet EMRIs in the present of gas around the MBH. Finally, the inclination diffusion can be also be relevant to other transients in nuclear clusters, such as tidal disruption events, since the loss cone also serves as a formation channel.

EMRI rates remain highly uncertain, and in this work we focus on one additional source of systematic uncertainty: the role of inclination diffusion in the presence of a spinning MBH. Our analysis was restricted to the loss-cone formation channel, however, the mathematical framework developed here for treating two-body scatterings in 3D is more general and may also be applicable to other EMRI formation channels, such as wet EMRIs in the presence of gas surrounding the MBH. Finally, inclination diffusion may also be relevant for other transients in galactic nuclei, such as tidal disruption events, for which loss-cone dynamics likewise play a central role (Stone et al. 2020).

## REFERENCES

- Abbott, B. P., Abbott, R., Abbott, T. D., et al. 2016, PhRvL, 116, 061102,  
doi: [10.1103/PhysRevLett.116.061102](https://doi.org/10.1103/PhysRevLett.116.061102)
- Abbott, R., Abbott, T. D., Acernese, F., et al. 2023, Physical Review X, 13, 041039,  
doi: [10.1103/PhysRevX.13.041039](https://doi.org/10.1103/PhysRevX.13.041039)
- Aharon, D., & Perets, H. B. 2016, ApJL, 830, L1,  
doi: [10.3847/2041-8205/830/1/L1](https://doi.org/10.3847/2041-8205/830/1/L1)
- Alexander, T. 2017, ARA&A, 55, 17,  
doi: [10.1146/annurev-astro-091916-055306](https://doi.org/10.1146/annurev-astro-091916-055306)
- Amaro-Seoane, P. 2018, Living Reviews in Relativity, 21, 4,  
doi: [10.1007/s41114-018-0013-8](https://doi.org/10.1007/s41114-018-0013-8)
- Amaro-Seoane, P., Sopuerta, C. F., & Freitag, M. D. 2013, MNRAS, 429, 3155, doi: [10.1093/mnras/sts572](https://doi.org/10.1093/mnras/sts572)
- Babak, S., Fang, H., Gair, J. R., Glampedakis, K., & Hughes, S. A. 2007, PhRvD, 75, 024005,  
doi: [10.1103/PhysRevD.75.024005](https://doi.org/10.1103/PhysRevD.75.024005)
- Babak, S., Gair, J., Sesana, A., et al. 2017, PhRvD, 95, 103012, doi: [10.1103/PhysRevD.95.103012](https://doi.org/10.1103/PhysRevD.95.103012)
- Bar-Or, B., & Alexander, T. 2016, ApJ, 820, 129,  
doi: [10.3847/0004-637X/820/2/129](https://doi.org/10.3847/0004-637X/820/2/129)
- Barausse, E., Berti, E., Hertog, T., et al. 2020, General Relativity and Gravitation, 52, 81,  
doi: [10.1007/s10714-020-02691-1](https://doi.org/10.1007/s10714-020-02691-1)

- Bardeen, J. M., Press, W. H., & Teukolsky, S. A. 1972, ApJ, 178, 347, doi: [10.1086/151796](https://doi.org/10.1086/151796)
- Binney, J., & Tremaine, S. 2008, Galactic Dynamics: Second Edition
- Bortolas, E., & Mapelli, M. 2019, MNRAS, 485, 2125, doi: [10.1093/mnras/stz440](https://doi.org/10.1093/mnras/stz440)
- Broggi, L., Bortolas, E., Bonetti, M., Sesana, A., & Dotti, M. 2022, MNRAS, 514, 3270, doi: [10.1093/mnras/stac1453](https://doi.org/10.1093/mnras/stac1453)
- Broggi, L., Stone, N. C., Ryu, T., et al. 2024, The Open Journal of Astrophysics, 7, 48, doi: [10.33232/001c.120086](https://doi.org/10.33232/001c.120086)
- Cohn, H., & Kulsrud, R. M. 1978, ApJ, 226, 1087, doi: [10.1086/156685](https://doi.org/10.1086/156685)
- Collins, N. A., & Hughes, S. A. 2004, PhRvD, 69, 124022, doi: [10.1103/PhysRevD.69.124022](https://doi.org/10.1103/PhysRevD.69.124022)
- Danzmann, K., & LISA Study Team. 1996, Classical and Quantum Gravity, 13, A247, doi: [10.1088/0264-9381/13/11A/033](https://doi.org/10.1088/0264-9381/13/11A/033)
- Derdzinski, A., & Mayer, L. 2023, MNRAS, 521, 4522, doi: [10.1093/mnras/stad749](https://doi.org/10.1093/mnras/stad749)
- Drasco, S., & Hughes, S. A. 2006, PhRvD, 73, 024027, doi: [10.1103/PhysRevD.73.024027](https://doi.org/10.1103/PhysRevD.73.024027)
- Gair, J. R., & Glampedakis, K. 2006, PhRvD, 73, 064037, doi: [10.1103/PhysRevD.73.064037](https://doi.org/10.1103/PhysRevD.73.064037)
- Generozov, A., Stone, N. C., Metzger, B. D., & Ostriker, J. P. 2018, MNRAS, 478, 4030, doi: [10.1093/mnras/sty1262](https://doi.org/10.1093/mnras/sty1262)
- Glampedakis, K., Hughes, S. A., & Kennefick, D. 2002, PhRvD, 66, 064005, doi: [10.1103/PhysRevD.66.064005](https://doi.org/10.1103/PhysRevD.66.064005)
- Greene, J. E., Strader, J., & Ho, L. C. 2020, ARA&A, 58, 257, doi: [10.1146/annurev-astro-032620-021835](https://doi.org/10.1146/annurev-astro-032620-021835)
- Gültekin, K., Richstone, D. O., Gebhardt, K., et al. 2009, ApJ, 698, 198, doi: [10.1088/0004-637X/698/1/198](https://doi.org/10.1088/0004-637X/698/1/198)
- Hailey, C. J., Mori, K., Bauer, F. E., et al. 2018, Nature, 556, 70, doi: [10.1038/nature25029](https://doi.org/10.1038/nature25029)
- Hils, D., & Bender, P. L. 1995, ApJL, 445, L7, doi: [10.1086/187876](https://doi.org/10.1086/187876)
- Hopman, C., & Alexander, T. 2005, ApJ, 629, 362, doi: [10.1086/431475](https://doi.org/10.1086/431475)
- . 2006, ApJ, 645, 1152, doi: [10.1086/504400](https://doi.org/10.1086/504400)
- Hopman, C., Freitag, M., & Larson, S. L. 2007, MNRAS, 378, 129, doi: [10.1111/j.1365-2966.2007.11758.x](https://doi.org/10.1111/j.1365-2966.2007.11758.x)
- Hughes, S. A., Warburton, N., Khanna, G., Chua, A. J. K., & Katz, M. L. 2021, PhRvD, 103, 104014, doi: [10.1103/PhysRevD.103.104014](https://doi.org/10.1103/PhysRevD.103.104014)
- Kaur, K., & Perets, H. B. 2024, ApJ, 977, 8, doi: [10.3847/1538-4357/ad89bd](https://doi.org/10.3847/1538-4357/ad89bd)
- Kaur, K., & Stone, N. C. 2025, ApJ, 979, 172, doi: [10.3847/1538-4357/ad9b86](https://doi.org/10.3847/1538-4357/ad9b86)
- Levin, Y. 2007, MNRAS, 374, 515, doi: [10.1111/j.1365-2966.2006.11155.x](https://doi.org/10.1111/j.1365-2966.2006.11155.x)
- Lightman, A. P., & Shapiro, S. L. 1977, ApJ, 211, 244, doi: [10.1086/154925](https://doi.org/10.1086/154925)
- Luo, J., Chen, L.-S., Duan, H.-Z., et al. 2016, Classical and Quantum Gravity, 33, 035010, doi: [10.1088/0264-9381/33/3/035010](https://doi.org/10.1088/0264-9381/33/3/035010)
- Mancieri, D., Broggi, L., Bonetti, M., & Sesana, A. 2025, A&A, 694, A272, doi: [10.1051/0004-6361/202452306](https://doi.org/10.1051/0004-6361/202452306)
- Mazzolari, G., Bonetti, M., Sesana, A., et al. 2022, MNRAS, 516, 1959, doi: [10.1093/mnras/stac2255](https://doi.org/10.1093/mnras/stac2255)
- Merritt, D. 2013, Dynamics and Evolution of Galactic Nuclei
- Miller, M. C., Freitag, M., Hamilton, D. P., & Lauburg, V. M. 2005, ApJL, 631, L117, doi: [10.1086/497335](https://doi.org/10.1086/497335)
- Naoz, S., Rose, S. C., Michaely, E., et al. 2022, ApJL, 927, L18, doi: [10.3847/2041-8213/ac574b](https://doi.org/10.3847/2041-8213/ac574b)
- Pan, Z., Lyu, Z., & Yang, H. 2021, PhRvD, 104, 063007, doi: [10.1103/PhysRevD.104.063007](https://doi.org/10.1103/PhysRevD.104.063007)
- Peters, P. C. 1964, Physical Review, 136, 1224, doi: [10.1103/PhysRev.136.B1224](https://doi.org/10.1103/PhysRev.136.B1224)
- Qunbar, I., & Stone, N. C. 2024, PhRvL, 133, 141401, doi: [10.1103/PhysRevLett.133.141401](https://doi.org/10.1103/PhysRevLett.133.141401)
- Rauch, K. P., & Tremaine, S. 1996, NewA, 1, 149, doi: [10.1016/S1384-1076\(96\)00012-7](https://doi.org/10.1016/S1384-1076(96)00012-7)
- Raveh, Y., & Perets, H. B. 2021, MNRAS, 501, 5012, doi: [10.1093/mnras/staa4001](https://doi.org/10.1093/mnras/staa4001)
- Reynolds, C. S. 2021, ARA&A, 59, 117, doi: [10.1146/annurev-astro-112420-035022](https://doi.org/10.1146/annurev-astro-112420-035022)
- Rom, B., Linial, I., Kaur, K., & Sari, R. 2024, ApJ, 977, 7, doi: [10.3847/1538-4357/ad8b1d](https://doi.org/10.3847/1538-4357/ad8b1d)
- Rosenbluth, M. N., MacDonald, W. M., & Judd, D. L. 1957, Physical Review, 107, 1, doi: [10.1103/PhysRev.107.1](https://doi.org/10.1103/PhysRev.107.1)
- Ryan, F. D. 1995, PhRvD, 52, 5707, doi: [10.1103/PhysRevD.52.5707](https://doi.org/10.1103/PhysRevD.52.5707)
- . 1997, PhRvD, 56, 1845, doi: [10.1103/PhysRevD.56.1845](https://doi.org/10.1103/PhysRevD.56.1845)
- Schnittman, J. D. 2015, ApJ, 806, 264, doi: [10.1088/0004-637X/806/2/264](https://doi.org/10.1088/0004-637X/806/2/264)
- Shapiro, S. L., & Marchant, A. B. 1978, ApJ, 225, 603, doi: [10.1086/156521](https://doi.org/10.1086/156521)
- Sigurdsson, S., & Rees, M. J. 1997, MNRAS, 284, 318, doi: [10.1093/mnras/284.2.318](https://doi.org/10.1093/mnras/284.2.318)
- Speri, L., Barsanti, S., Maselli, A., et al. 2024, arXiv e-prints, arXiv:2406.07607, doi: [10.48550/arXiv.2406.07607](https://doi.org/10.48550/arXiv.2406.07607)
- Spitzer, Jr., L., & Hart, M. H. 1971, ApJ, 164, 399, doi: [10.1086/150855](https://doi.org/10.1086/150855)
- Stone, N. C., Vasiliev, E., Kesden, M., et al. 2020, SSRv, 216, 35, doi: [10.1007/s11214-020-00651-4](https://doi.org/10.1007/s11214-020-00651-4)

- Sun, H., Li, Y.-P., Pan, Z., & Yang, H. 2025, arXiv e-prints, arXiv:2509.00469, doi: [10.48550/arXiv.2509.00469](https://doi.org/10.48550/arXiv.2509.00469)
- Teukolsky, S. A. 1973, ApJ, 185, 635, doi: [10.1086/152444](https://doi.org/10.1086/152444)
- Valiante, R., Colpi, M., Schneider, R., et al. 2021, MNRAS, 500, 4095, doi: [10.1093/mnras/staa3395](https://doi.org/10.1093/mnras/staa3395)
- Vasiliev, E., & Merritt, D. 2013, ApJ, 774, 87, doi: [10.1088/0004-637X/774/1/87](https://doi.org/10.1088/0004-637X/774/1/87)
- Yunes, N., Pani, P., & Cardoso, V. 2012, PhRvD, 85, 102003, doi: [10.1103/PhysRevD.85.102003](https://doi.org/10.1103/PhysRevD.85.102003)

## APPENDIX

## A. GENERAL GEODESIC DIFFUSION COEFFICIENTS

To calculate the diffusion coefficients, we follow the approach of Rosenbluth et al. (1957). We start with the local Cartesian velocity coordinates:

$$q^1 \equiv v = \sqrt{v_r^2 + v_\theta^2 + v_\phi^2}, \quad q^2 \equiv v_\theta, \quad q^3 \equiv v_\phi. \quad (\text{A1})$$

The corresponding metric tensor is:

$$a_{ij} = \begin{bmatrix} \left(\frac{v}{v_r}\right)^2 & \frac{-vv_\theta}{v_r^2} & \frac{-vv_\phi}{v_r^2} \\ \frac{-vv_\theta}{v_r^2} & \frac{v_r^2 + v_\theta^2}{v_r^2} & \frac{v_\theta v_\phi}{v_r^2} \\ \frac{-vv_\phi}{v_r^2} & \frac{v_\theta v_\phi}{v_r^2} & \frac{v_r^2 + v_\phi^2}{v_r^2} \end{bmatrix} \quad (\text{A2})$$

with the determinant:  $a \equiv \det(a_{ij}) = v^2/v_r^2 = v^2/(v^2 - v_\theta^2 - v_\phi^2)$ .

The invariant form of the Fokker-Planck equation is:

$$\begin{aligned} \left( \frac{\partial f}{\partial t} \right) &= - (f T^i)_{;i} + \frac{1}{2} (f S^{ij})_{;ij} \\ &= -a^{1/2} \left[ a^{1/2} f \left( T^i - \frac{1}{2} \Gamma_{jk}^i S^{jk} \right) \right]_{,i} + \frac{1}{2} a^{-1/2} \left[ a^{1/2} f S^{ij} \right]_{,ij} \end{aligned} \quad (\text{A3})$$

where the semicolons denote covariant differentiation and commas indicate simple derivatives.  $\Gamma_{jk}^i$  are the Christoffel symbols, and  $T^i$  and  $S^{ij}$  are the diffusion coefficients as tensorial objects:

$$T^i = \langle \Delta v^i \rangle = \Gamma' a^{ij} \frac{\partial \mathcal{H}}{\partial v^j} \quad (\text{A4a})$$

$$S^{ij} = \langle \Delta v^i \Delta v^j \rangle = \Gamma' \left[ a^{ik} a^{jl} \left( \frac{\partial^2 \mathcal{G}}{\partial v^k \partial v^l} - \Gamma_{kl}^m \frac{\partial \mathcal{G}}{\partial v^m} \right) \right] \quad (\text{A4b})$$

where  $\Gamma' = 4\pi G^2 \ln \Lambda$  and

$$\begin{aligned} \mathcal{H}(\vec{v}) &= \sum_b m_b (m + m_b) h_b(\vec{v}), \quad \mathcal{G}(\vec{v}) = \sum_b m_b^2 g_b(\vec{v}), \\ h_b(\vec{v}) &= \int \frac{f_b(\vec{v}_f)}{|\vec{v} - \vec{v}_f|} d\vec{v}_f, \quad g_b(\vec{v}) = \int f_b(\vec{v}_f) |\vec{v} - \vec{v}_f| d\vec{v}_f. \end{aligned} \quad (\text{A5})$$

The nonzero components of the Christoffel symbols:

$$\begin{aligned} \Gamma_{11}^1 &= -\frac{v_\theta^2 + v_\phi^2}{vv_r^2}, \quad \Gamma_{12}^1 = \Gamma_{21}^1 = \frac{v_\theta}{v_r^2}, \quad \Gamma_{13}^1 = \Gamma_{31}^1 = \frac{v_\phi}{v_r^2}, \\ \Gamma_{22}^1 &= -\frac{v^2 - v_\phi^2}{vv_r^2}, \quad \Gamma_{23}^1 = \Gamma_{32}^1 = \frac{v_\theta v_\phi}{vv_r^2}, \quad \Gamma_{33}^1 = -\frac{v^2 - v_\theta^2}{vv_r^2}. \end{aligned} \quad (\text{A6})$$

After substituting the metric and the Christoffel symbols from Eqs. (A2) and (A6) to Eq. (A4), we get these expressions for  $T^i$  and  $S^{ij}$ :

$$T^1 = \Gamma' \left( \frac{\partial \mathcal{H}}{\partial v} + \frac{v_\theta}{v} \frac{\partial \mathcal{H}}{\partial v_\theta} + \frac{v_\phi}{v} \frac{\partial \mathcal{H}}{\partial v_\phi} \right), \quad T^2 = \Gamma' \left( \frac{v_\theta}{v} \frac{\partial \mathcal{H}}{\partial v} + \frac{\partial \mathcal{H}}{\partial v_\theta} \right), \quad T^3 = \Gamma' \left( \frac{v_\phi}{v} \frac{\partial \mathcal{H}}{\partial v} + \frac{\partial \mathcal{H}}{\partial v_\phi} \right). \quad (\text{A7})$$

$$\begin{aligned}
S^{11} &= \Gamma' \left[ \frac{\partial^2 \mathcal{G}}{\partial v^2} + \left( \frac{v_\theta}{v} \right)^2 \frac{\partial^2 \mathcal{G}}{\partial v_\theta^2} + \left( \frac{v_\phi}{v} \right)^2 \frac{\partial^2 \mathcal{G}}{\partial v_\phi^2} + 2 \frac{v_\theta}{v} \frac{\partial^2 \mathcal{G}}{\partial v \partial v_\theta} + 2 \frac{v_\phi}{v} \frac{\partial^2 \mathcal{G}}{\partial v \partial v_\phi} + 2 \frac{v_\theta v_\phi}{v^2} \frac{\partial^2 \mathcal{G}}{\partial v_\theta \partial v_\phi} \right], \\
S^{22} &= \Gamma' \left[ \left( \frac{v_\theta}{v} \right)^2 \frac{\partial^2 \mathcal{G}}{\partial v^2} + \frac{\partial^2 \mathcal{G}}{\partial v_\theta^2} + 2 \frac{v_\theta}{v} \frac{\partial^2 \mathcal{G}}{\partial v \partial v_\theta} + \frac{v^2 - v_\theta^2}{v^3} \frac{\partial \mathcal{G}}{\partial v} \right], \\
S^{33} &= \Gamma' \left[ \left( \frac{v_\phi}{v} \right)^2 \frac{\partial^2 \mathcal{G}}{\partial v^2} + \frac{\partial^2 \mathcal{G}}{\partial v_\phi^2} + 2 \frac{v_\phi}{v} \frac{\partial^2 \mathcal{G}}{\partial v \partial v_\phi} + \frac{v^2 - v_\phi^2}{v^3} \frac{\partial \mathcal{G}}{\partial v} \right], \\
S^{12} &= \Gamma' \left[ \frac{v_\theta}{v} \frac{\partial^2 \mathcal{G}}{\partial v^2} + \frac{v_\theta}{v} \frac{\partial^2 \mathcal{G}}{\partial v_\theta^2} + \left( 1 + \left( \frac{v_\theta}{v} \right)^2 \right) \frac{\partial^2 \mathcal{G}}{\partial v \partial v_\theta} + \frac{v_\theta v_\phi}{v^2} \frac{\partial^2 \mathcal{G}}{\partial v \partial v_\phi} + \frac{v_\phi}{v} \frac{\partial^2 \mathcal{G}}{\partial v_\theta \partial v_\phi} \right], \\
S^{13} &= \Gamma' \left[ \frac{v_\phi}{v} \frac{\partial^2 \mathcal{G}}{\partial v^2} + \frac{v_\phi}{v} \frac{\partial^2 \mathcal{G}}{\partial v_\phi^2} + \frac{v_\theta v_\phi}{v^2} \frac{\partial^2 \mathcal{G}}{\partial v \partial v_\theta} + \left( 1 + \left( \frac{v_\phi}{v} \right)^2 \right) \frac{\partial^2 \mathcal{G}}{\partial v \partial v_\phi} + \frac{v_\theta}{v} \frac{\partial^2 \mathcal{G}}{\partial v_\theta \partial v_\phi} \right], \\
S^{23} &= \Gamma' \left[ \frac{v_\theta v_\phi}{v^2} \frac{\partial^2 \mathcal{G}}{\partial v^2} + \frac{v_\phi}{v} \frac{\partial^2 \mathcal{G}}{\partial v \partial v_\theta} + \frac{v_\theta}{v} \frac{\partial^2 \mathcal{G}}{\partial v \partial v_\phi} + \frac{\partial^2 \mathcal{G}}{\partial v_\theta \partial v_\phi} - \frac{v_\theta v_\phi}{v^3} \frac{\partial \mathcal{G}}{\partial v} \right].
\end{aligned} \tag{A8}$$

To transform the diffusion coefficients from the coordinates  $(v^1, v^2, v^3)$  to the coordinates  $(V^1, V^2, V^3)$  we can use:

$$\begin{aligned}
\langle \Delta V^\lambda \rangle &= V_{,i}^\lambda T^i + \frac{1}{2} V_{;ij}^\lambda S^{ij} = \frac{\partial V^\lambda}{\partial v^i} T^i + \frac{1}{2} \left( \frac{\partial^2 V^\lambda}{\partial v^i \partial v^j} - \frac{\partial V^\lambda}{\partial v^k} \Gamma_{ij}^k \right) S^{ij}, \\
\langle \Delta V^\mu \Delta V^\nu \rangle &= V_{,i}^\mu V_{,j}^\nu S^{ij} = \frac{\partial V^\mu}{\partial v^i} \frac{\partial V^\nu}{\partial v^j} S^{ij}.
\end{aligned} \tag{A9}$$

where the  $\mu, \nu, \lambda$  indices are associated with the new ( $V$ ) coordinate system and  $i, j, k$  with the old ( $v$ ) system.

Now we can transform the diffusion coefficients from  $(q^1, q^2, q^3)$  to  $(E, L_z, Q)$  using Eq. (A9):

$$\begin{aligned}
\langle \Delta E \rangle &= \Gamma' \left[ v \frac{\partial \mathcal{H}}{\partial v} + v_\theta \frac{\partial \mathcal{H}}{\partial v_\theta} + v_\phi \frac{\partial \mathcal{H}}{\partial v_\phi} + \frac{1}{2} \frac{\partial^2 \mathcal{G}}{\partial v^2} + \frac{1}{2} \frac{\partial^2 \mathcal{G}}{\partial v_\theta^2} + \frac{1}{2} \frac{\partial^2 \mathcal{G}}{\partial v_\phi^2} + \frac{v_\theta}{v} \frac{\partial^2 \mathcal{G}}{\partial v \partial v_\theta} + \frac{v_\phi}{v} \frac{\partial^2 \mathcal{G}}{\partial v \partial v_\phi} + \frac{1}{v} \frac{\partial \mathcal{G}}{\partial v} \right], \\
\langle (\Delta E)^2 \rangle &= \Gamma' \left[ v^2 \frac{\partial^2 \mathcal{G}}{\partial v^2} + v_\theta^2 \frac{\partial^2 \mathcal{G}}{\partial v_\theta^2} + v_\phi^2 \frac{\partial^2 \mathcal{G}}{\partial v_\phi^2} + 2vv_\theta \frac{\partial^2 \mathcal{G}}{\partial v \partial v_\theta} + 2vv_\phi \frac{\partial^2 \mathcal{G}}{\partial v \partial v_\phi} + 2v_\theta v_\phi \frac{\partial^2 \mathcal{G}}{\partial v_\theta \partial v_\phi} \right], \\
\langle \Delta L_z \rangle &= \Gamma' \left[ \frac{L_z}{v} \frac{\partial \mathcal{H}}{\partial v} + \frac{L_z}{v_\phi} \frac{\partial \mathcal{H}}{\partial v_\phi} \right], \\
\langle (\Delta L_z)^2 \rangle &= \Gamma' \left[ \left( \frac{L_z}{v} \right)^2 \frac{\partial^2 \mathcal{G}}{\partial v^2} + \left( \frac{L_z}{v_\phi} \right)^2 \frac{\partial^2 \mathcal{G}}{\partial v_\phi^2} + 2 \frac{L_z^2}{vv_\phi} \frac{\partial^2 \mathcal{G}}{\partial v \partial v_\phi} + \frac{L_z^2(v^2 - v_\phi^2)}{v^3 v_\phi^2} \frac{\partial \mathcal{G}}{\partial v} \right], \\
\langle \Delta Q \rangle &= \Gamma' \left\{ \left( -2 \frac{vE}{c^4} \cos^2 \theta a^2 + 2r^2 \frac{v_\theta^2}{v} + 2r^2 \cos^2 \theta \frac{v_\phi^2}{v} \right) \frac{\partial \mathcal{H}}{\partial v} + \left( -2 \frac{vE}{c^4} \cos^2 \theta a^2 \frac{v_\theta}{v} + 2r^2 v_\theta \right) \frac{\partial \mathcal{H}}{\partial v_\theta} \right. \\
&\quad + \left( -2 \frac{vE}{c^4} \cos^2 \theta a^2 \frac{v_\phi}{v} + 2r^2 \cos^2 \theta v_\phi \right) \frac{\partial \mathcal{H}}{\partial v_\phi} + \left[ r^2 \left( \frac{v_\theta}{v} \right)^2 + \cos^2 \theta \left( -a^2(E + v^2) + r^2 \left( \frac{v_\phi}{v} \right)^2 \right) \right] \frac{\partial^2 \mathcal{G}}{\partial v^2} \\
&\quad + \left( r^2 - a^2 \cos^2 \theta \frac{E + v_\theta^2}{c^4} \right) \frac{\partial^2 \mathcal{G}}{\partial v_\theta^2} + \left( r^2 \cos^2 \theta - a^2 \cos^2 \theta \frac{E + v_\phi^2}{c^4} \right) \frac{\partial^2 \mathcal{G}}{\partial v_\phi^2} + 2 \frac{v_\theta}{v} \left( r^2 - a^2 \frac{E + v^2}{c^4} \cos^2 \theta \right) \frac{\partial^2 \mathcal{G}}{\partial v \partial v_\theta} \\
&\quad + 2 \frac{v_\phi}{v} \cos^2 \theta \left( r^2 - a^2 \frac{E + v^2}{c^4} \right) \frac{\partial^2 \mathcal{G}}{\partial v \partial v_\phi} - 2a^2 \frac{v_\theta v_\phi}{c^4} \cos^2 \theta \frac{\partial^2 \mathcal{G}}{\partial v_\theta \partial v_\phi} \\
&\quad \left. + \frac{1}{v^3} \left( r^2(v^2 - v_\theta^2) + \cos^2 \theta (-2a^2 \frac{Ev^2}{c^4} + r^2(v^2 - v_\phi^2)) \right) \frac{\partial \mathcal{G}}{\partial v} \right\}, \\
\langle (\Delta Q)^2 \rangle &= \Gamma' \left\{ \frac{1}{v^2} \left[ -a^2 \frac{Ev^2}{c^4} + r^2(2v_\theta^2 + v_\phi^2) + \cos(2\theta)(-a^2 \frac{Ev^2}{c^4} + r^2 v_\phi^2) \right]^2 \frac{\partial^2 \mathcal{G}}{\partial v^2} \right. \\
&\quad + v_\theta^2 (2a^2 \frac{E}{c^4} \cos^2 \theta - 2r^2)^2 \frac{\partial^2 \mathcal{G}}{\partial v_\theta^2} + 4v_\phi^2 \cos^4 \theta (r^2 - a^2 \frac{E}{c^4})^2 \frac{\partial^2 \mathcal{G}}{\partial v_\phi^2} \\
&\quad + \frac{8}{v} \left[ r^4 v_\theta^3 + \cos^2 \theta (-a^2 \frac{E}{c^4} r^2 v^2 v_\theta - a^2 \frac{E}{c^4} r^2 v_\theta^3 + r^4 v_\theta v_\phi^2) + \cos^4 \theta (a^4 \frac{E^2}{c^8} v^2 v_\theta - a^2 \frac{E}{c^4} r^2 v_\theta v_\phi^2) \right] \frac{\partial^2 \mathcal{G}}{\partial v \partial v_\theta} \\
&\quad + \frac{8}{v} \left[ \cos^2 \theta (a^2 \frac{E}{c^4} r^2 v_\theta^2 v_\phi + r^4 v_\theta^2 v_\phi) + \cos^4 \theta (a^4 \frac{E^2}{c^8} v^2 v_\phi - a^2 \frac{E}{c^4} r^2 v^2 v_\phi - a^2 \frac{E}{c^4} r^2 v_\phi^3 + r^4 v_\phi^3) \right] \frac{\partial^2 \mathcal{G}}{\partial v \partial v_\phi} \\
&\quad + \left[ \cos^2 \theta (-8a^2 \frac{E}{c^4} r^2 v_\theta v_\phi + 8r^4 v_\theta v_\phi) + \cos^4 \theta (8a^4 \frac{E^2}{c^8} v_\theta v_\phi - 8a^2 \frac{E}{c^4} r^2 v_\theta v_\phi) \right] \frac{\partial^2 \mathcal{G}}{\partial v_\theta \partial v_\phi} \\
&\quad \left. + \frac{4r^4}{v^3} [v^2 v_\theta^2 - v_\theta^4 - 2v_\theta^2 v_\phi^2 \cos^2 \theta + \cos^4 \theta (v^2 v_\phi^2 - v_\phi^4)] \frac{\partial \mathcal{G}}{\partial v} \right\}, 
\end{aligned} \tag{A10}$$

and the cross terms:

$$\begin{aligned}
\langle \Delta E \Delta L_z \rangle &= \Gamma' \left[ L_z \frac{\partial^2 \mathcal{G}}{\partial v^2} + L_z \frac{\partial^2 \mathcal{G}}{\partial v_\phi^2} + L_z \frac{v_\theta}{v} \frac{\partial^2 \mathcal{G}}{\partial v \partial v_\theta} + L_z \frac{v^2 + v_\phi^2}{vv_\phi} \frac{\partial^2 \mathcal{G}}{\partial v \partial v_\phi} + L_z \frac{v_\theta}{v_\phi} \frac{\partial^2 \mathcal{G}}{\partial v_\theta \partial v_\phi} \right], \\
\langle \Delta E \Delta Q \rangle &= \Gamma' \left\{ \left[ 2r^2 v_\theta^2 + 2(-a^2 \frac{Ev^2}{c^4} + r^2 v_\phi^2) \cos^2 \theta \right] \frac{\partial^2 \mathcal{G}}{\partial v^2} + 2v_\theta^2 (r^2 - a^2 \frac{E}{c^4} \cos^2 \theta) \frac{\partial^2 \mathcal{G}}{\partial v_\theta^2} + 2v_\phi^2 (r^2 - a^2 \frac{E}{c^4}) \cos^2 \theta \frac{\partial^2 \mathcal{G}}{\partial v_\phi^2} \right. \\
&\quad + \frac{2v_\theta}{v} \left[ r^2 v^2 + r^2 v_\theta^2 + \cos^2 \theta (r^2 v_\phi^2 - 2a^2 \frac{Ev^2}{c^4}) \right] \frac{\partial^2 \mathcal{G}}{\partial v \partial v_\theta} + \frac{2v_\phi}{v} \left[ r^2 v_\theta^2 + \cos^2 \theta (r^2 v^2 + r^2 v_\phi^2 - 2a^2 \frac{Ev^2}{c^4}) \right] \frac{\partial^2 \mathcal{G}}{\partial v \partial v_\phi} \\
&\quad \left. + \left[ 2r^2 v_\theta v_\phi + 2v_\theta v_\phi \cos^2 \theta (r^2 - 2a^2 \frac{E}{c^4}) \right] \frac{\partial^2 \mathcal{G}}{\partial v_\theta \partial v_\phi} \right\}, \\
\langle \Delta L_z \Delta Q \rangle &= \Gamma' \left\{ \frac{2L_z}{v^2} \left[ r^2 v_\theta^2 + \cos^2 \theta (r^2 v_\phi^2 - a^2 \frac{Ev^2}{c^4}) \right] \frac{\partial^2 \mathcal{G}}{\partial v^2} + 2L_z \cos^2 \theta (r^2 - a^2 \frac{E}{c^4}) \frac{\partial^2 \mathcal{G}}{\partial v_\phi^2} \right. \\
&\quad + \frac{2L_z v_\theta}{v} (r^2 - a^2 \frac{E}{c^4} \cos^2 \theta) \frac{\partial^2 \mathcal{G}}{\partial v \partial v_\theta} + \frac{2L_z}{vv_\phi} \left[ r^2 v_\theta^2 - \cos^2 \theta (-2r^2 v_\phi^2 + a^2 \frac{E}{c^4} (v^2 + v_\phi^2)) \right] \frac{\partial^2 \mathcal{G}}{\partial v \partial v_\phi} \\
&\quad \left. + \frac{2L_z v_\theta}{v_\phi} (r^2 - a^2 \frac{E}{c^4} \cos^2 \theta) \frac{\partial^2 \mathcal{G}}{\partial v_\theta \partial v_\phi} - \frac{2L_z r^2}{v^3} [v_\theta^2 + (v_\phi^2 - v^2) \cos^2 \theta] \frac{\partial \mathcal{G}}{\partial v} \right\}.
\end{aligned} \tag{A11}$$

## B. ORBIT AVERAGED DIFFUSION COEFFICIENTS

The orbit-averaged diffusion coefficient,  $\langle \Delta V^i \rangle$  where  $V^i \in \{E, L_z, Q\}$ , is given by

$$\langle \Delta V^i \rangle_o \equiv \frac{\int_{\text{orb}} \langle \Delta V^i \rangle a^{1/2} \left| \frac{\partial(v, v_\theta, v_\phi)}{\partial(E, L_z, Q)} \right| d\vec{x}}{\int_{\text{orb}} a^{1/2} \left| \frac{\partial(v, v_\theta, v_\phi)}{\partial(E, L_z, Q)} \right| d\vec{x}} \tag{B12}$$

where  $a$  denotes the determinant of the metric from Eq. (A2), and  $\left| \frac{\partial(v, v_\theta, v_\phi)}{\partial(E, L_z, Q)} \right|$  is the Jacobian determinant of the coordinate transformation from  $(q^1 = v, q^2 = v_\theta, q^3 = v_\phi)$  to  $(E, L_z, Q)$ . Calculating the determinant of the metric and the Jacobian, we obtain:

$$a^{1/2} \left| \frac{\partial(v, v_\theta, v_\phi)}{\partial(E, L_z, Q)} \right| = \frac{v}{v_r} \frac{1}{2r^3 vv_\theta \sin \theta} = \frac{1}{2r^3 v_r v_\theta \sin \theta}. \tag{B13}$$

Since the local diffusion coefficients depend on  $r$  and  $\theta$ , the integration is:

$$\int_{\text{orb}} d\vec{x} = 2 \int_{\theta_{\min}}^{\theta_{\max}} \int_{r_p}^{r_a} 2\pi r^2 \sin \theta dr d\theta \tag{B14}$$

where  $r_p$  and  $r_a$  are the pericenter and apocenter, respectively, and  $\theta_{\min} = \pm(\pi/2 - I)$  and  $\theta_{\max} = \pi - \theta_{\min}$  are the minimum and maximum values of  $\theta$  along the orbit for a given inclination  $I$ , where the upper sign refers to prograde orbits, while the lower sign refers to retrograde orbits.

Combining Eqs. (B12) to (B14), the orbit averages are:

$$\langle \Delta V^i \rangle_o \equiv \frac{\int_{\theta_{\min}}^{\theta_{\max}} \int_{r_p}^{r_a} J \langle \Delta V^i \rangle dr d\theta}{\int_{\theta_{\min}}^{\theta_{\max}} \int_{r_p}^{r_a} J dr d\theta} \tag{B15}$$

where  $J = \frac{1}{rv_r v_\theta}$ .

When calculating the local diffusion coefficients, we assume that they are dominant near apocenter, far from the MBH. However, when performing the orbital average, we need to be more careful, since along the orbit the test particle approaches the MBH near pericenter, where relativistic effects can become important. For instance, the orbit undergoes precession, so  $\theta_{\min}$  and  $\theta_{\max}$  do not coincide with pericenter and apocenter. Consequently, the averaging

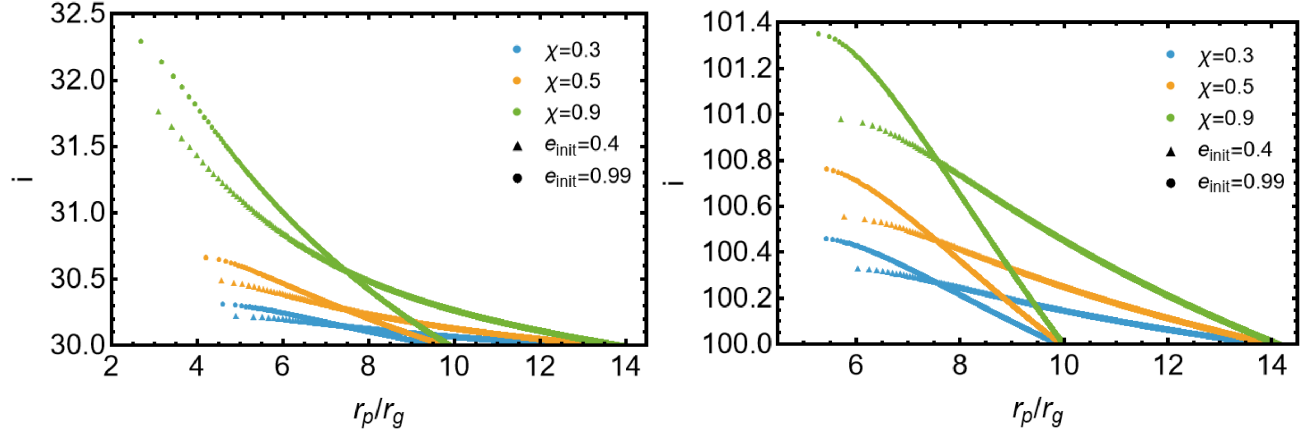


**Figure 6.** Inclination evolution as a function of pericenter radius due to GW emission calculated using Gair & Glampedakis (2006), for different MBH spins and initial orbital parameters. We can see only a small change in the orbital inclination.

should be carried out over geodesics rather than Keplerian orbits. In particular, the squared velocity  $v^2 = v_r^2 + v_\theta^2 + v_\phi^2$  is computed from the geodesic equations (Bardeen et al. 1972) where:

$$\begin{aligned} v_r^2 &= \dot{r}^2 = R(r)/\Sigma(r, \theta)^2 \\ v_\theta^2 &= r^2 \dot{\theta}^2 = r^2 \Theta(\theta)/\Sigma(r, \theta)^2 \\ v_\phi^2 &= r^2 \sin^2 \theta \dot{\phi}^2 = r^2 \sin^2 \theta \Phi(r, \theta)/\Sigma(r, \theta)^2 \end{aligned} \quad (\text{B16})$$

where the derivatives are with respect to proper time,  $R(r)$ ,  $\Theta(\theta)$  and  $\Phi(r, \theta)$  are the radial, polar and azimuthal potentials of the Kerr metric, and  $\Sigma = r^2 + \chi^2 \cos^2 \theta$ . The integrand prefactor is therefore  $J = \frac{\Sigma(r, \theta)^2}{r^2 \sqrt{R(r)} \sqrt{\Theta(\theta)}}$ . Also, we note that the integration boundaries are the roots of the respective potentials.

Additionally, we tested the accuracy of using the Newtonian form of this Jacobian:  $J = [(2(E - c^2 - \Phi(r)) - L_z^2/r^2 - Q/r^2)(Q - L_z^2 \cot^2 \theta)]^{-1/2}$  and found that the deviation from the geodesic result is small.

### C. GRAVITATIONAL WAVES LOSSES

In this paper, we compute the GW fluxes using the “kludge” method described in Gair & Glampedakis (2006). To check the impact of the GWs on the orbital inclination, we compute the orbital evolution driven solely by GW emission. In Fig. 6, we present the evolution of the orbital inclination and find that it changes only weakly over the course of the inspiral. This indicates that the inclination evolution calculated in this work is primarily driven by inclination diffusion due to two-body scatterings rather than by GW emission. In addition, we compare the approach of Gair & Glampedakis (2006) with that of Peters (1964). We find in Fig. 7 that the differences between the two methods become relevant only close to the MBH, where GW emission has already circularized the orbit.

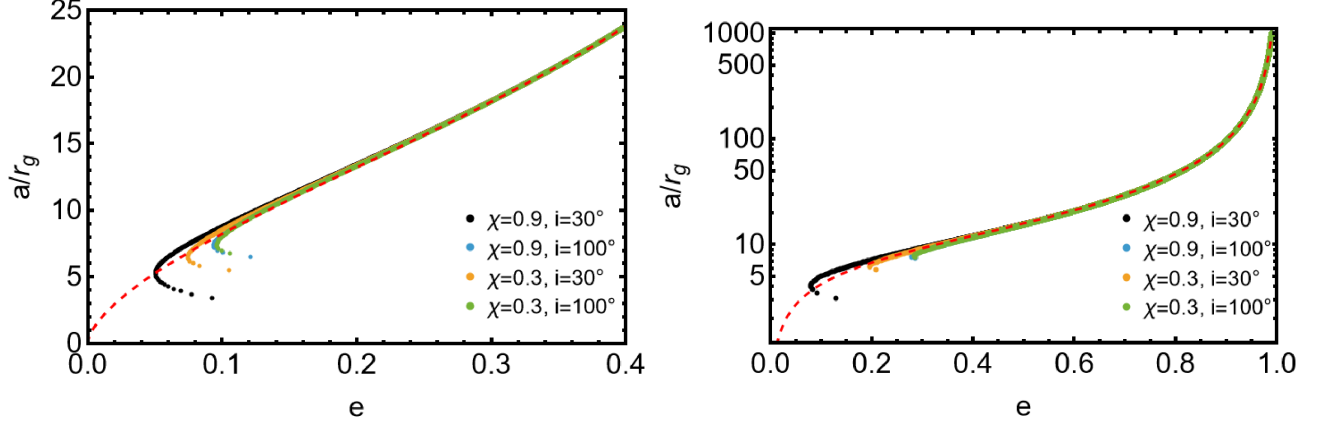


**Figure 7.** Comparisons between the semimajor axis as a function of eccentricity between Gair & Glampedakis (2006) (colored solid curves) and Peters (1964) (red dashed curve). The comparisons are presented for different MBH spins, and initial semimajor axes, eccentricities and inclinations.